Electrochemical Impedance Analysis of Symmetrical Ni/Gadolinium-Doped Ceria (CGO10) Electrodes in Electrolyte-Supported Solid Oxide Cells

Matthias Riegraf,[1,z] Rémi Costa,[1] Günter Schiller,[1] K. Andreas Friedrich,[1,2] Sebastian Dierickx,[3] and André Weber[3,*]

[1]*German Aerospace Centre (DLR), Institute of Engineering Thermodynamics, 70569 Stuttgart, Germany*
[2]*University of Stuttgart, Institute of Building Energetics, Thermal Engineering and Energy Storage (IGTE), Pfaffenwaldring 31, 70569 Stuttgart, Germany*
[3]*Karlsruhe Institute of Technology (KIT), Institute for Applied Materials (IAM-WET), 76131 Karlsruhe Germany*

One of the most powerful tools in solid oxide cell (SOC) characterization is electrochemical impedance spectroscopy, which can unfold important insights into SOC performance characteristics and degradation behavior. To obtain a better understanding of the electrochemical behavior of Ni/CGO fuel electrodes, this work presents a comprehensive investigation of state-of-the-art Ni/CGO10-based electrolyte-supported cells. Commercial Ni/CGO10|CGO10|3YSZ|CGO10|Ni/CGO10 symmetrical cells were characterized between 550–975°C at $pH_2 = 0.8$ bar and $pH_2O = 0.2$ bar, and for different H_2/H_2O gas mixtures at 550°C. (i) Small electrode area, (ii) thin electrodes and (iii) large gas flow rates were used to minimize mass transport contributions. Based on distribution of relaxation times (DRT) analysis an equivalent circuit model was derived. Electrode process contributions on Ni/CGO were determined by means of a complex non-linear least square fit of the equivalent circuit model to the experimental data. One low frequency process at 0.1–1 Hz and one middle frequency process at 10–100 Hz were identified and correlated to a surface and a bulk process, respectively. Values for the apparent activation energy barriers and reaction orders with respect to steam and hydrogen content were determined.
 [DOI: 10.1149/2.0051913jes]

Manuscript submitted June 11, 2019; revised manuscript received July 22, 2019. Published August 7, 2019.

The transition to energy systems based on the use of more renewable energy is accompanied by an increasing mismatch between production and demand, which leads to a growing demand for electric energy storage systems. In this regard, the solid oxide cell (SOC) technology promises high round-trip efficiencies toward the electrolysis of steam into hydrogen which can be stored as energy carrier, and its reutilization by conversion into steam while producing emission-free electricity. One commonly used cell architecture in commercial applications is the electrolyte-supported cell (ESC) design due to its excellent mechanical stability.[1] The fuel electrodes of choice for both fuel cell and electrolysis mode are the nickel/yttria-stabilized zirconia (YSZ) and the nickel/gadolinium-based ceria (CGO) electrode.[2–4]

Important insights into the kinetics of the Ni/YSZ electrode have been achieved via the use of electrochemical impedance spectroscopy (EIS) in symmetrical and full cell configurations.[5–9] This is facilitated by occurrence of the Ni/YSZ charge transfer process during hydrogen oxidation at high frequencies of 10^3–10^4 Hz,[10] which enables its clear separation from the lower frequency process of the LSM or LSCF cathode ($\sim 10^2$ Hz) and mass transport (10^0–10^1 Hz) contributions.[5,6,9–12] Based on EIS measurements and the calculation of the distribution of relaxation times (DRT), the process resistances can be determined by means of a complex non-linear least square (CNLS) fit of experimental data to a physically meaningful equivalent circuit model (ECM). Then, by means of systemic investigation of the dependencies of the process resistance contributions on temperature and gas phase composition, conclusions about the performance and degradation of individual cell components could be deduced and important insights into the mechanistic electrode behavior could be obtained.

However, this approach has been proven to be more complex for $Ni/Ce_{0.9}Gd_{0.1}O_{2-\delta}$(CGO10)-based cells due to the occurrence of a low frequency electrode process at ~1 Hz, and therefore the overlapping of anode, cathode, and mass transport contributions with similar relaxation frequencies.[3,13] In a recent study, the polarization resistance of different types of Ni/CGO-electrodes was investigated and compared with a state of the art anode-supported cell. The DRT analysis of the spectra revealed that the relaxation frequency of the main fuel electrode electrochemistry process was shifted from ~2 kHz (Ni/YSZ) to 3–10 Hz (Ni/CGO10).[14] This low frequency process was attributed to a surface process, most likely the electrode charge transfer reaction.[13] Its low frequency was correlated with the occurrence of a large chemical capacitance that originates from the oxygen non-stoichiometry of CGO. This non-stoichiometry is the reason for the mixed ionic and electronic conductivity (MIEC) properties of CGO at high temperature and reducing atmosphere,[15–17] which was suggested to cause its high performance and resistivity against sulfur poisoning and coking.[3,13,18–20]

In addition to a low frequency process, a middle frequency process at 10^2 Hz has been observed in impedance spectra as well which was suggested to originate from the oxide ion transport from bulk to surface or across the electrolyte/electrode interface.[21,22] However, a systematic study investigating state-of-the-art Ni/CGO10 symmetrical cells has not been carried out yet.

Therefore, in the present study the loss mechanisms in Ni/CGO10 fuel electrodes are identified and their contributions are separated by means of the combination of EIS, DRT and a CNLS fit to a developed ECM model. Symmetrical, electrolyte-supported cells are used in order to avoid the convolution of fuel and air electrode. Furthermore, small electrode areas, thin electrodes and large gas flow rates were employed to minimize mass transport contributions.

Experimental

All symmetrical cell measurements were carried out with a commercial, state-of-the-art electrolyte-supported cell with dimensions of 12 × 12 mm² and an active surface area of 10 × 10 mm² (Kerafol, Germany). 25 µm thick Ni/CGO10 electrodes were applied onto a 90 µm thick 3 mol% YSZ (3YSZ) electrolyte, that was coated with 5 µm thick CGO10 adhesion layers on both sides. While 8 mol % Y_2O_3 stabilized zirconia (8YSZ) is often used as electrolyte material in anode-supported cell architectures due to higher ionic conductivity, 3 mol % YSZ is frequently preferred as substrate in electrolyte-supported cells due to higher mechanical stability.[23] Furthermore, the electrodes contain a current collector layer with increased Ni content. A scanning electron microscopy (SEM) image of a typical

*Electrochemical Society Member.
[z]E-mail: Matthias.Riegraf@dlr.de

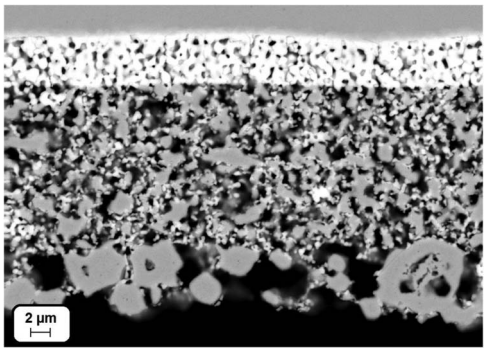

Figure 1. An SEM image of a reduced Ni/CGO10 electrode reference cell.

electrode is depicted in Figure 1. Full cells with the same fuel electrode were characterized in detail by means of current-voltage characteristics and electrochemical impedance spectroscopy in our previous publications.[13,18,24]

The cell was mounted in a ceramic cell housing as depicted in Figure 2 and contacted with Ni meshes on both sides.[5] As a one-atmosphere setup was employed no sealing between the electrodes was required. The atmosphere in the reactive chamber consisted of $H_2/H_2O/N_2$ gas mixtures and its composition was measured via a lambda sensor close to the sample. Electrochemical impedance spectroscopy measurements were carried out at OCV to determine the cell resistance.

Symmetrical cell measurements are presented that were carried out in the symmetrical cell setup depicted in Figure 2. Hydrogen partial pressure, steam partial pressure and temperature were varied independently of each other. The cell was tested in a temperature range between 550– 975°C at steps of 25 K and at $pH_2 = 0.8$ bar and $pH_2O = 0.2$ bar. Hydrogen partial pressure was varied between 0.08 – 0.80 bar at constant $pH_2O = 0.2$ bar and at 550°C, and the steam partial pressure was varied between 0.08 – 0.42 bar at constant $pH_2 = 0.4$ bar and at 550°C. The rest of the fuel gas consisted of nitrogen. Total gas flow rates were kept constant at 1 L·min^{-1}. An overview of the measured operating conditions in this study is given in Table I. The combined use of symmetrical cells, small electrode areas, thin electrodes and large gas flow rates is employed to minimize mass transport contributions. This approach was shown to reduce both the gas conversion and the gas diffusion impedance in the employed setup to a minimum.[5]

Impedance spectroscopy was carried out using a Solartron 1260 FRA (frequency response analyzer) at frequencies between 10 mHz and 1 MHz. The current amplitudes were chosen for the voltage response not to exceed 12 mV.[25] A Kramers Kronig Test was applied to the data to ensure the validity of the measured spectra.[26]

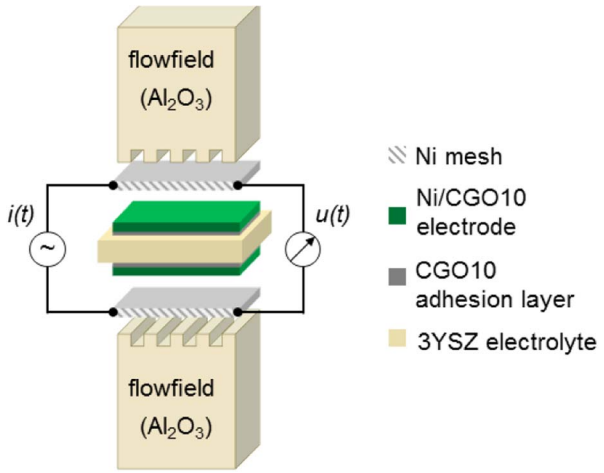

Figure 2. Schematic illustration of the sample holder in the symmetrical cell test bench.

Table I. Operating conditions of the EIS measurements. Fuel gas composition and temperature were varied independently. All measurements were recorded at OCV with a flow rate of 1 L·min^{-1}.

Temperature T/°C	Steam partial pressure pH_2O/bar	Hydrogen partial pressure pH_2/bar	Nitrogen partial pressure pN_2/bar
550			
575			
600			
625			
650			
675			
700			
725			
750	↑	↑	↑
	0.8	0.2	0.0
775	↓	↓	↓
800			
825			
850			
875			
900			
925			
950			
975			
	0.08		0.52
↑	0.14	↑	0.46
	0.18		0.42
550		0.4	
	0.22		0.38
↓	0.28	↓	0.32
	0.36		0.24
	0.46		0.14
	0.6		0
		0.08	0.72
		0.14	0.66
		0.18	0.62
↑	↑	0.22	0.58
550	0.2		
		0.28	0.52
		0.36	0.44
↓	↓	0.46	0.34
		0.6	0.2

The impedance spectra were evaluated with an ECM developed below. The fit proceeds via a CNLS method. In the CNLS fitting procedure the DRT was used as a third variable alongside the real and imaginary parts. ECM used for this procedure were developed by calculating and analyzing the DRT of the impedance spectra.[27]

Results and Discussion

In the following, the characterization of the symmetrical cells and their analysis by means of electrochemical impedance spectroscopy is shown. The behavior of the Ni/CGO electrode is systematically investigated by independent variation of temperature, pH_2O and pH_2.

Temperature dependence.—Figure 3 shows a typical EIS measurement at a temperature of 550°C. Two distinguished arcs can be identified, one with a peak frequency of ∼0.5 Hz and the other with a peak frequency of ∼10 Hz. Furthermore, the beginning of an additional arc is indicated at frequencies higher than 10^4 Hz. This high frequency arc corresponds to the resistance within the electrolyte and thus, the

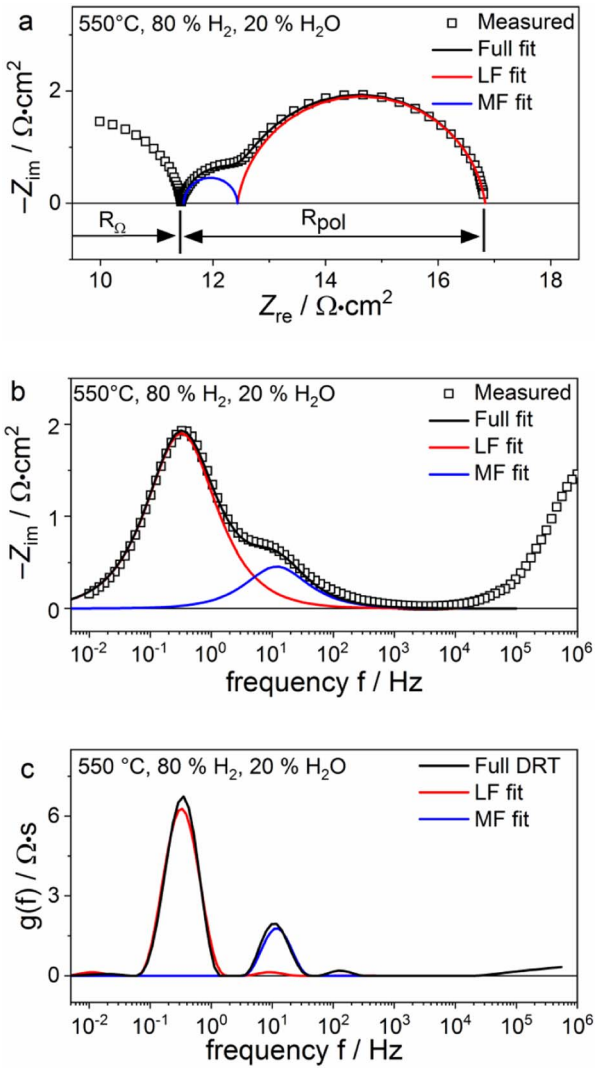

Figure 3. (a) Nyquist, (b) imaginary impedance, (c) and DRT plots at 550°C. The gas phase composition was $pH_2 = 0.8$ bar and $pH_2O = 0.2$ bar. Points indicate the experimental and lines the simulated data. Blue, red and black lines denote the middle frequency process, low frequency process and the full impedance, respectively. The data shown in (c) denote the DRT of the measured impedance (black line), the DRT of the fitted low frequency process (red) and the DRT of the fitted middle frequency process (blue). Note that for the creation of the blue MF and the red LF line the resistance of the respectively other process was assumed to be 0. To obtain the black full fit in Figure 3a, the imaginary impedance values are added at every frequency value and not at every real impedance value, thus explaining the different trajectory of the full fit and the connected low frequency and middle frequency lines.

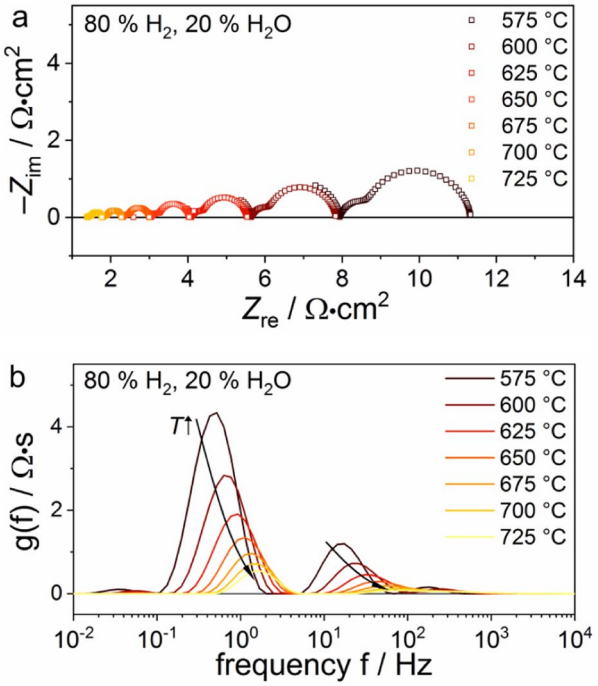

Figure 4. (a) Nyquist and (b) DRT plots for changing operating temperatures between 575–725°C. Measurements at higher temperatures were omitted here to increase visibility of the remaining plots. The gas phase composition was kept constant at $pH_2 = 0.8$ bar and $pH_2O = 0.2$ bar.

interception with the y-axis at ~11.5 Ω·cm^2 represents the value of the ohmic resistance. As polycrystalline electrolytes are employed, contributions of the YSZ grain bulk and YSZ grain boundaries appear in the high frequency range at low temperatures such as 550°C.[28] Furthermore the interdiffusion zone between CGO and YSZ might contribute to this process due to its lower conductivity. However, in the measured frequency range they cannot be fully resolved. These contributions become decreasingly visible at higher temperature and therefore are typically not reported in literature. The polarization resistance shows two nearly ideal semicircles.

The DRT calculated for the EIS measurements of the symmetrical cells at 0.8 bar H_2 and 0.2 bar H_2O and between 575–725°C is shown in Figure 4. The discussion of DRT has shown the potential to reveal significantly more insight into the cell behavior than raw impedance data as demonstrated in numerous previous publications.[5,6,8,29,30] The calculated DRT suggests two main contributions, one at low frequencies (LF) around 1 Hz and another at middle frequencies (MF) around 10^2 Hz, which is consistent with previous studies on Ni/CGO10 electrodes.[22,31] No high frequency contribution $>10^3$ Hz is visible as it is generally observed for Ni/YSZ electrodes.[5,6] Both of the contributions are thermally activated as suggested by the shift to lower frequencies with decreasing temperature, and thus, can be attributed to physico-chemical electrode processes. At lower temperatures (<650°C), another middle frequency contribution is visible at 10^2–10^3 Hz. However, as it is negligibly small the two middle frequency elements were therefore modeled with a single RQ element during the CNLS fitting process.

As it was not the focus of this study to resolve the high-frequency capacitive behavior of the electrolyte that is visible at lower temperatures (see Figure 3), the higher frequencies ($>10^4$ Hz) were omitted during the fitting processes and modeled by one simple resistance element that describes the ohmic resistance in electrolyte and adhesion layers. As a result, a simple ECM was applied that includes one resistance element and two RQ elements describing the two electrode processes. An exemplary fit is depicted for the impedance spectra in Figure 3 and demonstrates that the devised ECM matches the experimental data very well.

For Ni/YSZ fuel electrodes, a transmission line model has been shown to provide a more physically meaningful description of the electrode processes, modeling the coupling between ionic conduction pathway in the ceramic electrolyte matrix, electronic conduction pathway in the nickel phase and electrochemical reaction at the triple phase boundary.[5,8,9,32] This coupling is generally visible as a skewed semicircle with a linear shape at high frequencies that evolves into an attached semicircle at lower frequencies. However, since in this case the two processes do not seem to be coupled as clearly separated semicircles are present, a transmission line model cannot be applied without further detailed insights into the electrode mechanism.

The obtained resistance values of the two processes as a function of temperature are depicted in Figure 5. Apparent activation energy barriers for the processes can be extracted by fitting the data to the

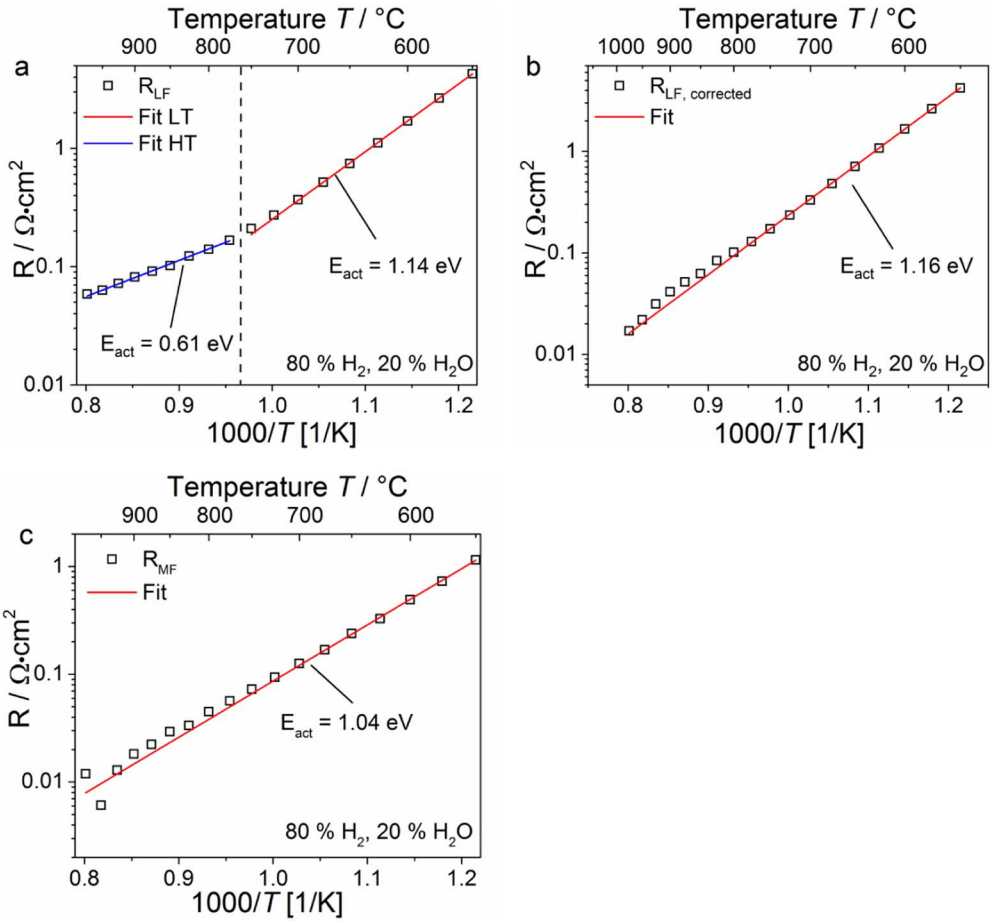

Figure 5. Resistance of (a) the low frequency electrode process, (b) the low frequency process with a subtracted gas diffusion resistance and (c) the middle frequency electrode process as a function of temperature *T*. All fits achieved values with a coefficient of determination $R^2 > 0.999$.

Arrhenius-type equation:

$$R_p(T) = B \exp(\frac{E_{act}}{RT}), \quad [1]$$

where R_p is the process resistance, B the pre-exponential factor and E_{act} the process, apparent activation energy barrier. The fit of the middle frequency process in Figure 5c shows a high quality (R^2 >0.999) and yields an apparent activation energy barrier of 1.04 eV. The fit for the low frequency process, however, shows a change of slope of the fitted curve (Figure 5a), and, therefore, two temperature regimes with different apparent activation energy barriers. Above 775°C, the apparent activation energy barrier is identified to be 0.61 eV, below 775°C it is 1.14 eV.

This difference in activation energy is most likely related to a gas diffusion resistance. Although the experiments in the present study have been carried out at OCV, the gas diffusion resistance can become non-negligible at higher temperatures. However, this does not mean that the cell operates in fuel starvation mode, but rather that the Nernst voltage across the cell is changing during the sinusoidal current excitation of the impedance measurements due to formation or consumption of hydrogen and steam at the electrode/electrolyte interface and their diffusive transport away from the interface.[34]

In a previous study of a nanoscaled high performance cathode it has been shown that the total polarization resistance is significantly increased by gas diffusion at temperatures exceeding 700°C.[33] After subtracting the gas diffusion resistance the remaining polarization resistance of the cathode electrochemistry showed a straight slope in the Arrhenius diagram that could properly be described by one single activation energy.

In case of the Ni/CGO electrodes investigated here, the gas diffusion polarization process cannot be resolved in the DRT as it is strongly overlapped by the other polarization processes. To overcome this problem, the gas diffusion resistance was taken from previous investigations performed on Ni/YSZ electrodes in exactly the same test bench.[5] A gas diffusion resistance of 41 mΩ·cm² was observed for similar testing conditions (950°C, 80% H_2O, 20% H_2). The temperature dependence of the gas diffusion resistance in 1D can be calculated according to

$$R_{diff} = \left(\frac{RT}{2F}\right)^2 \cdot d \cdot \left(\frac{1}{D_{\text{eff,H2}} \cdot p\text{H}_2} + \frac{1}{D_{\text{eff,H2O}} \cdot p\text{H}_2\text{O}}\right). \quad [2]$$

Here, R_{diff} is the gas diffusion resistance, R the universal gas constant, T the temperature, F the Faraday number, and d the distance.

Porous electrodes with a thickness below 30 µm have been suggested to exhibit a negligible gas diffusion resistance.[34] Thus, the observed values are not related to the porous electrode itself but to gas diffusion in the contact mesh and in-plane diffusive transport underneath the contact ribs.[5] Hence, the use of the gas diffusion resistance extracted from previous experiments is valid despite the differences in porosity and tortuosity between the Ni/CGO and the Ni/YSZ electrodes. Since the porosity of the employed Ni meshes is large, porous transport through the Ni meshes can solely be described by free molecular diffusion and Knudsen diffusion can be neglected.

Thus, the effective diffusion coefficients $D_{\text{eff,H2}}$ and $D_{\text{eff,H2O}}$ for hydrogen and steam, respectively, equal the binary diffusion coefficients and were calculated using the Chapman-Enskog theory proportionally to $T^{1.5}$.[35] This leads to a dependence of the gas diffusion resistance on $T^{0.5}$. The resulting values are then subtracted from the fitted

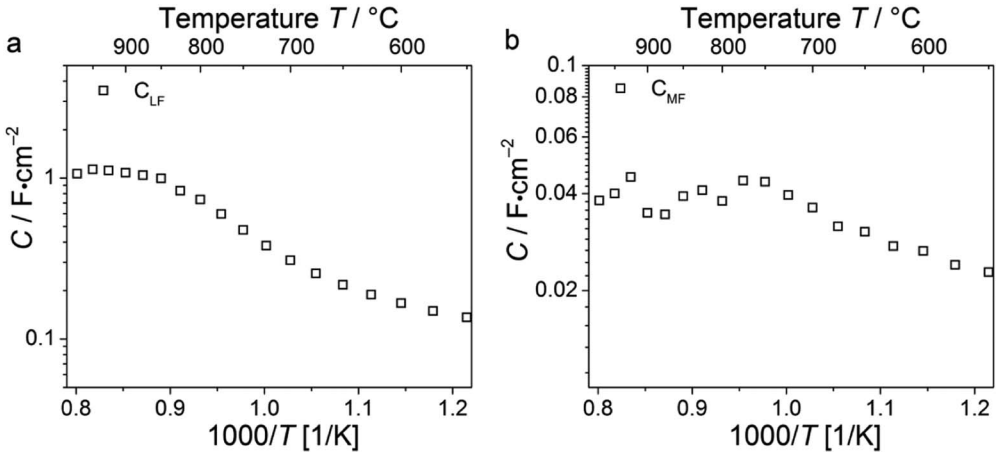

Figure 6. Capacitance of (a) the low frequency electrode process and (b) the middle frequency fuel electrode process as a function of temperature.

polarization resistance which leads to the corrected resistance values R_{LF} displayed in Fig. 4b. The corresponding fit of Eq. 1 to the experimental data shows excellent agreement over the whole temperature range with an apparent activation energy barrier of 1.16 eV.

Different possible fuel oxidation mechanisms were extensively discussed in our previous work, and the possibility of competitive pathways at double phase and triple phase boundary was pointed out.[13,18,24] These competitive pathways very likely exhibit different activation energy barriers.[36] However, as the whole temperature regime can readily be described by one activation energy barrier after correction of the low frequency resistance, the presence of two temperature regimes with different dominant fuel oxidation pathways can be considered unlikely. Thus, the rate-determining step probably stays the same over the whole temperature range. Its identification is beyond the scope of this study.

Figure 6a displays the capacitance values associated with the low frequency process. The values of about ~1 F·cm^{-2} are significantly larger than the ones generally obtained for Ni/YSZ (~10^{-4} F·cm^{-2}),[37,38] which clearly illustrates the different nature of the capacitance in Ni/CGO. The origin is likely a large chemical capacitance, which is associated with a changing Ce^{3+}/Ce^{4+} (correlated with a variation in the oxygen stoichiometry in the CGO phase) ratio in the CGO.[16,39,40] Although a convolution of the low frequency electrode process and the gas diffusion possibly exists in the present study, at low temperatures the cell behavior is expected to be dominated by the electrode process. The calculated capacitance values increase with temperature and exhibit plateaus at high and low temperatures. Thus, the Ce^{3+}/Ce^{4+} ratio determines the chemical capacitance values which stretch over a whole order of magnitude (0.1–1 F·cm^{-2}). Plateau formation occurs at conditions when further Ce^{3+} or Ce^{4+} formation is highly unfavorable. This quantitatively confirms an effect that we already qualitatively observed in sulfur poisoning experiments of Ni/CGO electrodes in our recent work and can explain the lower capacitance values of the surface process in Ni/CGO40 electrodes since the higher Gd doping level of CGO40 entails a higher concentration of intrinsic but lower concentration of extrinsic oxygen vacancies and thus, displays a less pronounced oxygen non-stoichiometry.[13]

The capacitance of the middle frequency process also shows a similar dependence on the temperature with increasing values (0.02–0.04 F·cm^{-2}) at higher temperatures, however, in a less pronounced manner.

All identified dependencies of resistance and capacitance values on the operating conditions are also shown in Table II.

pH_2O dependence.—In order to investigate the dependence of the electrode processes of fuel humidification, the steam content was varied between 0.08 and 0.6 bar at a constant hydrogen partial pressure of 0.4 bar and at a constant temperature of 550°C. This comparatively low temperature was chosen to minimize the influence of the gas diffusion and gas conversion process on the low frequency contribution.[12,34] Based on the gas diffusion resistance derived from previous measurements as explained above, it will account for only approximately ~0.8% (0.034 Ω·cm^2/4.25 Ω·cm^2) of the total resistance of the low frequency process R_{LF} at 550°C. The impedance and DRT plots in Figures 7a–7b reveal a significant dependence of the low frequency process on the steam content, while the middle frequency contribution was only marginally affected. This is consistent with previous studies.[13,22,31] The clear reduction of the low frequency electrode process resistance with increasing steam content suggests

Table II. Overview of the electrode processes identified in this study and their dependence on temperature, steam partial pressure and hydrogen partial pressure. A downwards-pointing arrow indicates a decrease in Resistance *R* or capacitance *C* upon an increase in operating parameter. Analogously, an upwards-pointing arrow indicates an increase.

Process	Characteristic frequency	Value	*T* dependence	pH_2O dependence	pH_2 dependence
Low frequency surface process	0.2–2 Hz	*R*	↓ $E_{act} = 1.16$ Ev	↓ ~$pH_2O^{-0.08}$ (*)	↓ ~$pH_2O^{-0.01}$ (**)
		C	↑	↓ ~$pH_2O^{-0.16}$	↑ ~$pH_2^{-0.11}$
Middle frequency bulk process	10–100 Hz	*R*	↓ $E_{act} = 1.04$ eV	–	–
		C	↑	–	–

(*) Fit with a coefficient of determination $R^2 = 0.67$, (**) $R^2 = 0.47$.

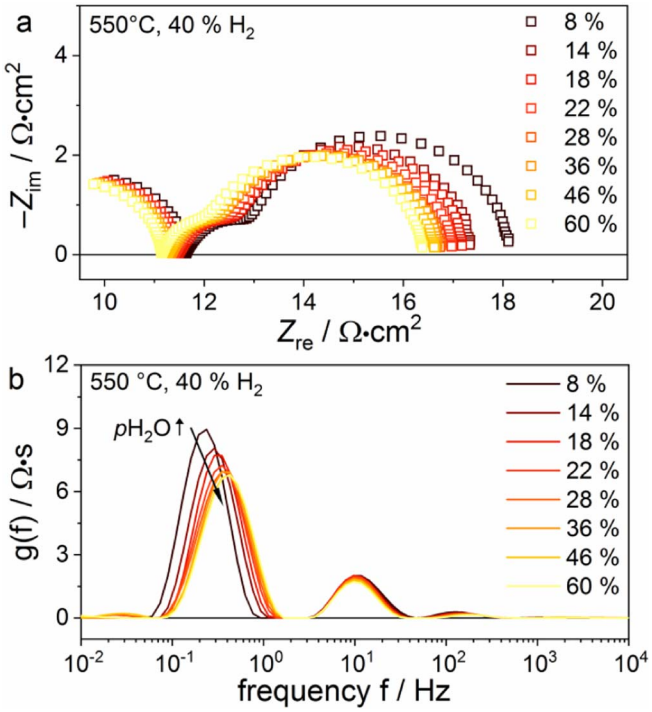

Figure 7. a) Nyquist and b) DRT plots of impedance measurements at changing hydrogen partial pressure (constant $pH_2 = 0.2$ bar). The temperature was kept constant at $T = 550$°C.

an enhancing effect of steam on the kinetics of the low frequency process, similar to the influence of H_2O on the electrode charge transfer process on Ni/YSZ.[6,37,38] This confirms that its origin is an electrode surface process (either at the CGO surface or at the TPB), probably the charge transfer process, as was already suggested in earlier publications.[16,20,31,41,42] In a MIEC material like CGO this will create a electrostatic surface potential step between charged adsorbates and electronic counter charges in the outmost surface layer of CGO.[40,43]

The small pH_2O dependence of the middle frequency process points toward a bulk process as its origin. Specifically, oxide ion transport from CGO bulk to surface or across the electrolyte/electrode interface has been suggested before.[21,22] In the former case, an electrostatic potential drop forms at the CGO/YSZ interface between electrolyte and adhesion layer. The latter process corresponds to the electrostatic potential drop between MIEC bulk and its surface which drives carrier transport in the space-charge layer.[40] However, within the framework of the present study it is difficult to distinguish between these processes.

For small overpotentials, the plot of the resistance of the electrode processes over the respective partial pressures on a double-logarithmic scale can be used to identify the dependencies of the resistance on pH_2 and pH_2O. The negative slopes of the diagrams then represent the reaction orders a and b of the electrode process with respect to the partial pressure of hydrogen and steam, respectively. In Figure 8a, the resistance of the low frequency process is plotted over pH_2O. The slope of the fit to the low frequency resistance in the double-logarithmic plane leads to the identification of $b = 0.08$. This is significantly smaller than the value calculated for the charge transfer process on Ni/YSZ ($b = 0.33$). The poor quality of the fit ($R^2 = 0.67$) could possibly be related to the the cell design, since based on the operating conditions, the electrochemically active zone can extend from the electrode functional layer into the electrode contact layer.[9] In addition, hydrogen oxidation could also occur in the not fully dense CGO adhesion layer. Thus, the interplay between the ionic conductivity in the matrix, the electrochemical hydrogen oxidation reaction and the gas diffusion can vary considerably. To further investigate these effects, an electrode with a more homogeneous layer structure could be helpful.

The capacitance values of the low frequency process obtained by the CNLS fit show a dependence on the steam partial pressure as well (Figure 8b) with a decreasing value for increasing pH_2O. The relationship at this temperature can be readily described with a power law according to $C_{LF} \sim pH_2O^{-0.16}$.

pH_2 dependence.—Eventually, to investigate the dependence of the electrode process on the hydrogen partial pressure, pH_2 was varied between 0.08 and 0.42 bar at a constant steam content of 0.2 bar and at 550°C. The Nyquist and DRT plot of the recorded impedance spectra are depicted in Figures 9a–9b. Again, the middle frequency contribution shows no dependence on the gas phase composition. Moreover, the low frequency peak also only shows a very small change upon hydrogen concentration variation.

The resistance and capacitance values of the process are depicted in Figure 10. Based on the fitting results in the double-logarithmic plot in Figure 10a, a reaction order value of $a = 0.01$ could be derived. Although the fit quality is poor ($R^2 = 0.47$), Figure 10a shows the nearly negligible influence of pH_2 on the surface process resistance. As the rate-determining step is probably the charge transfer reaction,[42] this means that independently of the hydrogen inlet content, hydrogen is always readily available on the surface as a reactant. Thus, hydrogen adsorption and dissociation are fast and probably do not strongly influence the hydrogen oxidation rate. The resistance dependence of the electrode process on temperature can be readily described by the Arrhenius-type equation in Eq. 1 without a change of slope in Figure 5b. This indicates that the rate-determining step does not change

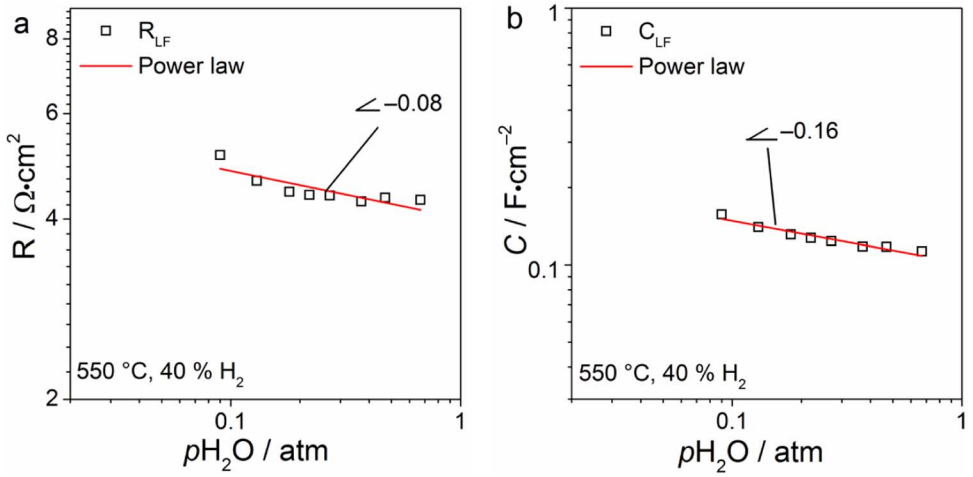

Figure 8. (a) Resistance and (b) capacitance of the low frequency electrode process as a function of pH_2O. The linear fits achieve (a) $R^2 = 0.67$ and (b) $R^2 = 0.92$.

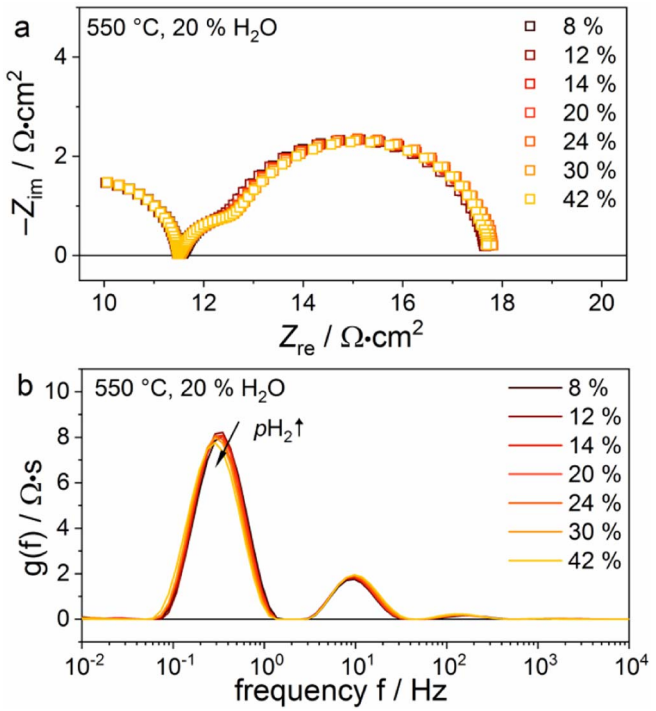

Figure 9. a) Nyquist and b) DRT plots of impedance measurements at changing hydrogen partial pressure (constant $pH_2 = 0.2$ bar). The temperature was kept constant at $T = 550$°C.

with an increase in temperature. Thus, the dependencies of the process on pH_2 and pH_2O are likely to be similar at higher temperatures as well. However, based on Figure 5 alone, it cannot be excluded that there are two competitive pathways with only slightly different apparent activation energy barriers that dominate under different operating conditions. The resistance contributions of the different elementary kinetic steps cannot be resolved within the scope of the present study. Extensive ab initio calculations and elementary kinetic modeling would be necessary to obtain more detailed insights into the reaction mechanism.

Furthermore, Figure 10b shows that the capacitance of the low frequency electrode process is also dependent on pH_2, with $C_{LF} \sim pH_2^{0.11}$. Thus, a dependence of the low frequency process on both temperature and pO_2 (caused by different pH_2O/pH_2 ratios) is confirmed. This can be correlated with previous investigations of CGO10, where the Ce^{3+} concentration in the CGO bulk was shown to change with both temperature and pO_2. This confirms the source of the capacitance to be related to the Ce^{3+}/Ce^{4+} ratio.

Conclusions

This work presents a comprehensive electrochemical impedance study of state-of-the-art Ni/CGO10-based electrolyte-supported cells. Commercial Ni/CGO10|CGO10|3YSZ-based symmetrical cells were characterized between 550–975°C at $pH_2 = 0.8$ bar and $pH_2O = 0.2$ bar and for different H_2/H_2O gas mixtures at 550°C. By employing small electrode areas, thin electrodes and large gas flow rates the effect of mass transport contributions was minimized to clearly identify and separate the electrode process. By means of calculating the DRT, an equivalent circuit model was derived comprising two RQ elements to model the electrode behavior. Electrode process contributions of Ni/CGO and their dependencies on the operating conditions were calculated by means of a complex non-linear least square fit of the equivalent circuit model to experimental data. One low frequency and one middle frequency electrode process were identified and correlated to a surface and a bulk process. Apparent activation energy barriers and the pH_2O and pH_2 dependencies of both processes were determined. Moreover, the capacitance of the Ni/CGO10 charge transfer process was shown to exhibit a significant dependence on both the operating temperature and gas phase composition. This reflects the existence of a large chemical capacitance with a changing Ce^{3+} concentration in CGO.

Acknowledgments

We gratefully acknowledge financial support by the German Ministry of Education and Research within the framework of the project "SOFC-Degradation: Analyse der Ursachen und Entwicklung von Gegenmaßnahmen" via grant numbers 03SF0494C and 03SF0494F.

ORCID

Matthias Riegraf https://orcid.org/0000-0002-0383-2545
Rémi Costa https://orcid.org/0000-0002-3534-1935
K. Andreas Friedrich https://orcid.org/0000-0002-2968-5029

References

1. S. C. Singhal and K. Kendall, *High-temperature Solid Oxide Fuel Cells: Fundamentals, Design and Applications*, Elsevier, Oxford, UK (2003).
2. A. Mai, B. Iwanschitz, U. Weissen, R. Denzler, D. Haberstock, V. Nerlich, J. Sfeir, and A. Schuler, *ECS Trans.*, **25**(1), 149 (2009).
3. M. Kusnezoff, N. Trofimenko, M. Müller, and A. Michaelis, *Materials*, **9**, 906 (2016).
4. A. Glauche, T. Betz, and M. Ise, *ECS Trans.*, **5**(2), 157 (2011).
5. V. Sonn, A. Leonide, and E. Ivers-Tiffée, *J. Electrochem. Soc.*, **155**, B675 (2008).

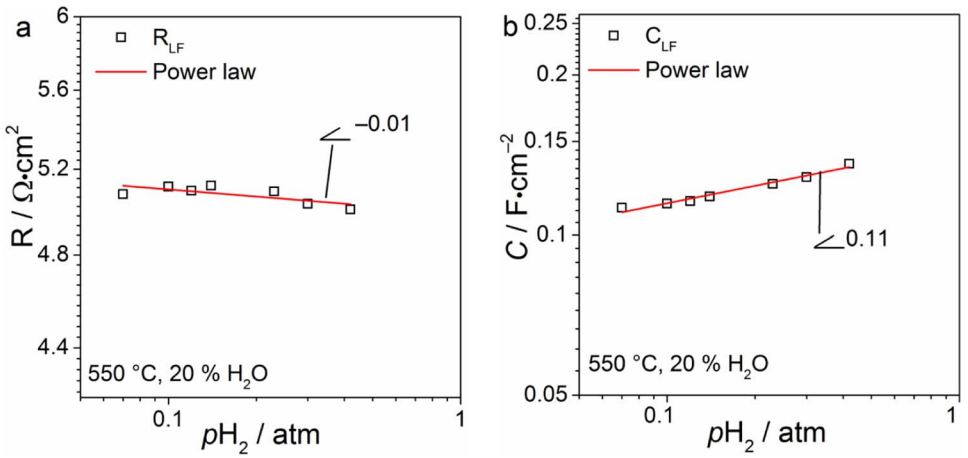

Figure 10. (a) Resistance and (b) capacitance of the low frequency electrode process as a function of pH_2. The linear fits achieve (a) $R^2 = 0.47$ and (b) $R^2 = 0.97$.

6. A. Leonide, V. Sonn, A. Weber, and E. Ivers-Tiffée, *J. Electrochem. Soc.*, **155**, B36 (2007).
7. A. Hagen, R. Barfod, P. V. Hendriksen, Y.-L. Liu, and S. Ramousse, *J. Electrochem. Soc.*, **153**, A1165 (2006).
8. S. Dierickx, J. Joos, A. Weber, and E. Ivers-Tiffée, *Electrochim. Acta*, **265**, 736 (2018).
9. S. Dierickx, T. Mundloch, A. Weber, and E. Ivers-Tiffée, *J. Power Sources*, **415**, 69 (2019).
10. A. Kromp, A. Leonide, A. Weber, and E. Ivers-Tiffée, *J. Electrochem. Soc.*, **158**, B980 (2011).
11. M. P. Hoerlein, M. Riegraf, R. Costa, G. Schiller, and K. A. Friedrich, *Electrochim. Acta*, **276**, 162 (2018).
12. W. G. Bessler and S. Gewies, *J. Electrochem. Soc.*, **154**, B548 (2007).
13. M. Riegraf, V. Yurkiv, R. Costa, G. Schiller, and K. A. Friedrich, *ChemSusChem*, **10**, 587 (2017).
14. A. Weber, S. Dierickx, N. Russner, and E. Ivers-Tiffée, *ECS Trans.*, **77**(10), 141 (2017).
15. C. Zhang, M. E. Grass, A. H. McDaniel, S. C. Decaluwe, F. El Gabaly, Z. Liu, K. F. McCarty, R. L. Farrow, M. A. Linne, Z. Hussain, G. S. Jackson, H. Bluhm, and B. W. Eichhorn, *Nat. Mater.*, **9**, 944 (2010).
16. T. Nakamura, T. Kobayashi, K. Yashiro, A. Kaimai, T. Otake, K. Sato, J. Mizusaki, and T. Kawada, *J. Electrochem. Soc.*, **155**, B563 (2008).
17. W. C. Chueh, Y. Hao, W. Jung, and S. M. Haile, *Nat. Mater.*, **11**, 155 (2012).
18. M. Riegraf, M. P. Hoerlein, R. Costa, G. Schiller, and K. A. Friedrich, *ACS Catal.*, **7**, 7760 (2017).
19. P. Boldrin, E. Ruiz-Trejo, J. Mermelstein, J. M. Bermúdez Menéndez, T. Ramírez Reina, and N. P. Brandon, *Chem. Rev.*, **116**, 13633 (2016).
20. W. C. Chueh, Y. Hao, W. Jung, and S. M. Haile, *Nat. Mater.*, **11**, 155 (2012).
21. S. Primdahl and Y. L. Liu, *J. Electrochem. Soc.*, **149**, A1466 (2002).
22. S. Primdahl and M. Mogensen, *Solid State Ionics*, **152–153**, 597 (2002).
23. S. P. S. Badwal and J. Drennan, *J. Mater. Sci.*, **22**, 3231 (1987).
24. M. Riegraf, A. Zekri, M. Knipper, R. Costa, G. Schiller, and K. A. Friedrich, *J. Power Sources*, **380**, 26 (2018).
25. D. Klotz, A. Weber, and E. Ivers-Tiffée, *Electrochim. Acta*, **227**, 110 (2017).
26. M. Schönleber, D. Klotz, and E. Ivers-Tiffée, *Electrochim. Acta*, **131**, 20 (2014).
27. H. Schichlein, A. C. Müller, M. Voigts, A. Krügel, and E. Ivers-Tiffée, *J. Appl. Electrochem.*, **32**, 875 (2002).
28. J. Nielsen and J. Hjelm, *Electrochim. Acta*, **115**, 31 (2014).
29. A. Weber, S. Dierickx, A. Kromp, and E. Ivers-Tiffée, *Fuel Cells*, **13**, 487 (2013).
30. A. Kromp, S. Dierickx, A. Leonide, A. Weber, and E. Ivers-Tiffée, *J. Electrochem. Soc.*, **159**, B597 (2012).
31. P. Kim, D. J. L. Brett, and N. P. Brandon, *J. Power Sources*, **189**, 1060 (2009).
32. B. A. Boukamp, *Electrochim. Acta*, **154**, 35 (2015).
33. C. Peters, A. Weber, and E. Ivers-Tiffée, *J. Electrochem. Soc.*, **155**, B730 (2008).
34. S. Primdahl and M. Mogensen, *J. Electrochem. Soc.*, **146**, 2827 (1999).
35. S. Chapman and T. G. Cowling, *The mathematical theory of non-uniform gases. 3rd edition*, Cambridge University Press, Cambridge, UK, (1991).
36. J. Nielsen, T. Klemenso, and P. Blennow, *J. Power Sources*, **219**, 305 (2012).
37. M. Vogler, A. Bieberle-Hütter, L. Gauckler, J. Warnatz, and W. G. Bessler, *J. Electrochem. Soc.*, **156**, B663 (2009).
38. W. G. Bessler, M. Vogler, H. Störmer, D. Gerthsen, A. Utz, A. Weber, and E. Ivers-Tiffée, *Phys. Chem. Chem. Phys.*, **12**, 13888 (2010).
39. J. Fleig, *Phys. Chem. Chem. Phys.*, **7**, 2027 (2005).
40. W. C. Chueh and S. M. Haile, *Annu. Rev. Chem. Biomol. Eng.*, **3**, 313 (2012).
41. L. Zhang, S. P. Jiang, H. Q. He, X. Chen, J. Ma, and X. C. Song, *Int. J. Hydrogen Energy*, **35**, 12359 (2010).
42. Z. A. Feng, F. El Gabaly, X. Ye, Z. X. Shen, and W. C. Chueh, *Nat. Commun.*, **5**, 1 (2014).
43. J. Fleig, *Phys. Chem. Chem. Phys.*, **7**, 2027 (2005).